연구논문

Effect of Critical Cooling Rate on the Formation of Intermetallic Phase During Rapid Solidification of FeNbHfBPC Alloy

Song-Yi Kim*, Hye-Ryeong Oh**, A-Young Lee*,***, Haneul Jang*, Seok-Jae Lee****,

Hwi-Jun Kim* and Min-Ha Lee*,*****,†

*Advanced Process and Materials R&D Group, Korea Institute of Industrial Technology, Incheon 21999, Republic of Korea
**Electronic Convergence Materials & Device Research Center, Korea Electronics Technology Institute,
Seongnam 13509, Republic of Korea
***Department of Functional Ceramics, Korea Institute of Materials Science, Changwon 51508, Republic of Korea
****Division of Advanced Materials Engineering, Research Center for Advanced Materials Development, Chonbuk National University,
Jeonju 54896, Republic of Korea
*****KITECH North America, Korea Institute of Industrial Technology, San Jose, CA 95134, USA

초 록

진공 가스분사법으로 제조된 $Fe_{75}B_{13}P_5Nb_2Hf_1C_4$ 합금의 응고중 액상의 크기와 이에 따른 냉각속도의 변화가 정출상의 형성에 미치는 영향에 대한 고찰을 하였다. 고온 액상에서 동일한 조건으로 응고된 서로 다른 크기의 액상이 구형의 분말형태로 응고될 때 크기에 따른 임계냉각속도의 차이를 계산하였으며, 액상의 평균 반지름이 3배정도 크기 차이가 날 경우 고상으로 변태할 때 임계냉각속도가 13.5배까지 차이가 나는 것을 알 수 있었다. 이러한 임계냉각 속도의 차이에 따른 정출상의 형성과 정출상의 형태와 크기에 따른 탄화물의 형성 거동을 조사하여 열역학 계산으로 예측된 결과와 비교 분석하였으며, 분말입자의 크기가 20~45 마이크론일 경우 Hf과 Nb이 포함된 MC타입의 탄화물이 초정으로 형성 되는 것을 알 수 있었으며 이때 Hf과 Nb의 비율은 합금의 조성 및 냉각속도에 따라 변화됨을 관찰 할 수 있었다.

핵심용어; 임계냉각속도, 급속응고, 분말입자, 비정질, 핵생성.

Abstract

We present the effect of the critical cooling rate during rapid solidification on the nucleation of precipitates in an $Fe_{75}B_{13}P_5Nb_2Hf_1C_4$ (at.%) alloy. The thermophysical properties of the rapidly solidified $Fe_{75}B_{13}P_5Nb_2Hf_1C_4$ liquids, which were obtained at various cooling rates with various sizes of gas-atomized powder during a high-pressure inert gas-atomization process, were evaluated. The cooling rate of the small-particle powder (≤ 20 μm) was 8.4×10^5 K/s, which was 13.5 times faster than that of the large-particle powder (20 to 45 mm; 6.2×10^4 K/s) under an atomized temperature. A thermodynamic calculation model used to predict the nucleation of the precipitates was confirmed by the microstructural observation of MC-type carbide in the $Fe_{75}B_{13}P_5Nb_2Hf_1C_4$ alloy. The primary carbide phase was only formed in the large-particle gas-atomized powder obtained during solidification at a slow cooling rate compared to that of the small-particle powder.

Key words; Critical cooling rate, Rapid solidification, Powder atomization, Amorphous and Nucleation.

1. Introduction

The nucleation of a solid phase from a liquid melt during solidification is a well-studied and well-understood phenomenon [1]. An understanding of the effect of transformation parameters, such as temperature distribution or cooling rate, between the crystallographic and non-crystallographic states of metals (i.e., solidification and melting) is important for controlling the physical properties of metals [1]. Generally, the formation of crystals during solidification is observed during relatively fast cooling, such as in melt spinning or gas atomization, owing to a secure time window for the freezing-phase transformation [2,3]. However, we also observe nucleated crystals resulting from the inevitable growth state by latent heat generation during solidification [1]. To minimize the growth effect of latent heat during the liquid to solid transformation, rapid solidification was introduced by solidifying the melt at a supercooled liquid or amorphous state, which has a similar atomic structure to liquid, resulting in less difference between the transformation enthalpy and latent heat [3,4].

Liquids at temperatures below their melting points are called supercooled liquids (SCLs) [5]. It was reported that fast cooling of a supercooled liquid below the glass transition temperature (T_g) can produce a glass [5]. Debenedetti et al. discussed the interpretation of supercooling and glass-formation phenomena by introducing the potential energy landscape concept [5]. Georgarakis et al. experimentally measured structural changes in the supercooled liquid region during cooling by in situ high-energy X-ray analysis [6]. Lee et al. presented magnetic property changes at different cooling rates during solidification [2].

In the current study, we evaluated the critical cooling rate of an $Fe_{75}B_{13}P_5Nb_2Hf_1C_4$ alloy with the formation of a primary intermetallic phase in frozen liquid melts with different cooling rates by high-pressure gas atomization.

2. Experimental Procedure

An Fe-based alloy with a nominal composition of $Fe_{75}B_{13}P_5Nb_2Hf_1C_4$ (at.%) was selected, which exhibits a supercooled liquid state with relatively high stability [2]. To obtain a monolithic phase vitrified with different cooling rates, we introduced a high-pressure gas-atomization method using heated N_2 gases at elevated temperature (500°C) as cooling media. The induction-melted pre-alloyed ingots were inductively re-melted in a MgO crucible under an Ar atmosphere for high-pressure gas atomization. The total weight of the feedstock material was 5 kg. The melt temperature was 1873 K before atomization started, followed by ejection with a gas overpressure of 50 bar. Nitrogen gas with a heat exchanger was used at a temperature of 773 K. The ejection temperatures were measured to be 1601 K (1328°C) for gas atomization. The chamber pressure was maintained at 1.2 bar and the oxygen content was 302-309 ppm, the detail of experimental procedures was reported elsewhere [2].

3. Results and Discussion

As a result of gas atomization, we obtained two different sizes of amorphous powders with sizes under 20 μm and 20-45 μm, respectively. The fast-cooled powder (≤20 μm) resulted in a fully glassy state, and the slow-cooled powder (20-45 μm) froze to include primary crystals. The atomization conditions, such as melt shooting temperature and oxygen content, were carefully controlled to maintain identical conditions to minimize the effect of other parameters. Normally, Fe-based amorphous powders under 45 μm in diameter produced by high-pressure gas atomization became fully amorphous. However, in the current study, amorphous powders less than 20 μm in diameter were used to confirm the intrinsic amorphous phase. There was a crystalline phase mixed in the amorphous powder with a diameter of 20-45 μm.

Fig. 1(a) shows the time-temperature-transformation schematic diagram of the solidification of the amorphous alloys with two different sizes which based on C_p data from DSC analysis. During solidification, the liquid was cooled to vitrify into the supercooled liquid region (DT_x) without crystallization. The smaller size powder (≤20 μm) followed fast cooling, which was necessary to avoid the crystallization nose. On the contrary, the larger powder (20-45 μm) followed slow cooling, which was in contact with the crystallization curve, resulting in the formation of a primary phase.

The effect of gas-atomization parameters (droplet temperature, melt superheat temperature, gas pressure, etc.) on the cooling rate was evaluated by Zheng et al. [7]. The cooling rate decreased with increasing flight time during gas atomization, and it also increased with decreasing
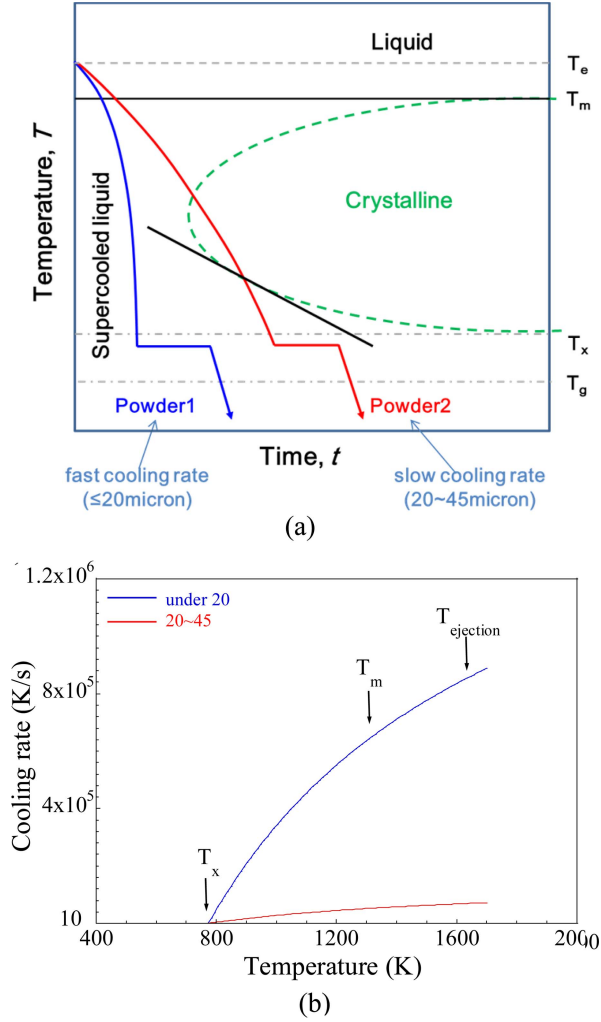
Fig. 1. (a) The time-temperature-transformation (TTT) diagram comparing the solidification pathway of gas-atomized powders of different sizes as a function of cooling rate. (b) Change of the cooling rate for fast-cooled small-sized powder (≤20 μm) and slow-cooled large-sized powder (20-45 μm) during high-pressure gas atomization.

droplet size. In this study, we considered that the calculation of cooling rates is dependent on the powder size, the temperature difference between the molten droplet and the ambient, the thermal conductivity, the specific heat capacity of the melt, and the atomizing gas [2].

The cooling rate change based on the measured C_p results during gas atomization by N_2 gas can be estimated using thermodynamic expressions. Assuming that the heat transfer between a spherical liquid droplet and the nitrogen gas medium during gas atomization can be described by a Newtonian formulation of cooling [8], the cooling rate of

spherical droplets related to diameter can be estimated from [9]

$$\frac{dT_d}{dt} = \frac{6(T_{ejection} - T_{gas})h}{dC_{pd}},\qquad(1)$$

where the heat transfer coefficient (h) is given as

$$h = 2\frac{K_d}{d} + 0.6\left(\frac{u}{d}\right)^{\frac{1}{2}}\left(K_d{}^2 C_{pg}\right)^{\frac{1}{3}}\left(\frac{\rho_g}{\mu_g}\right)^{\frac{1}{6}},\qquad(2)$$

Here, K_d is the thermal conductivity of the droplet, u is the relative gas/droplet velocity (approximately equal to zero at the freezing point of the liquid droplet as it becomes a solid particle during the gas-atomization process), $T_{ejection}$ is the melt temperature at the start of atomization, T_{gas} is the gas temperature, C_{pd} is the specific heat capacity of the droplets, C_{pg} is the specific heat capacity of the gas (1,039 J/kgK for nitrogen), ρ_g is the density of the gas (0.437 kg/m^3 for nitrogen at 500ºC), μ_g is the viscosity of the gas (35.08×10^{-6} Ns/m^2 for nitrogen at 500ºC), and d is the diameter of the droplets [7,8]. From Equations (1) and (2), it is apparent that the cooling rate in the liquid state is proportional to $1/d^2$, which shows the strong dependence of the cooling rate on the powder size d and the thermal conductivity K [7,8]. Equation (1) is simplified as follows:

$$\frac{dT_d}{dt} = \frac{12}{\rho C_{pd}}(T_d - T_f)\frac{K_g}{d^2},\qquad(3)$$

where K_g is the thermal conductivity of nitrogen gas (2.6× 10^{-2} W/mK), T_d is the droplet temperature ($T_d \approx T_{ejection}$ at the start of atomization; 1601 K), T_f is the gas temperature (773 K for nitrogen gas), ρ is the density of droplets (ρ = 7.431 kg/m^3), and C_{pd} is the specific heat capacity of the droplets for the Fe-based amorphous alloys [10, 11].

As shown in Fig. 1(b), the cooling rate difference between the small powder particles (≤20 μm in diameter) and the large powder particles (20-45 μm in diameter) during vitrification to each temperature from the liquid melt was clearly observed. The representative diameters of the droplets to calculate the cooling curves for the small-sized powder and large-sized powder were 10 μm and 32.5 μm, respectively. At the initial stage of gas atomization, the relative cooling rate difference between the small-sized powder (8.4×10^5 K/s) and the large-sized powder (6.2×10^4 K/s) around $T_{ejection}$ = 1601 K (1328ºC) was 13.5. The cooling rate of the small-sized powder was significantly
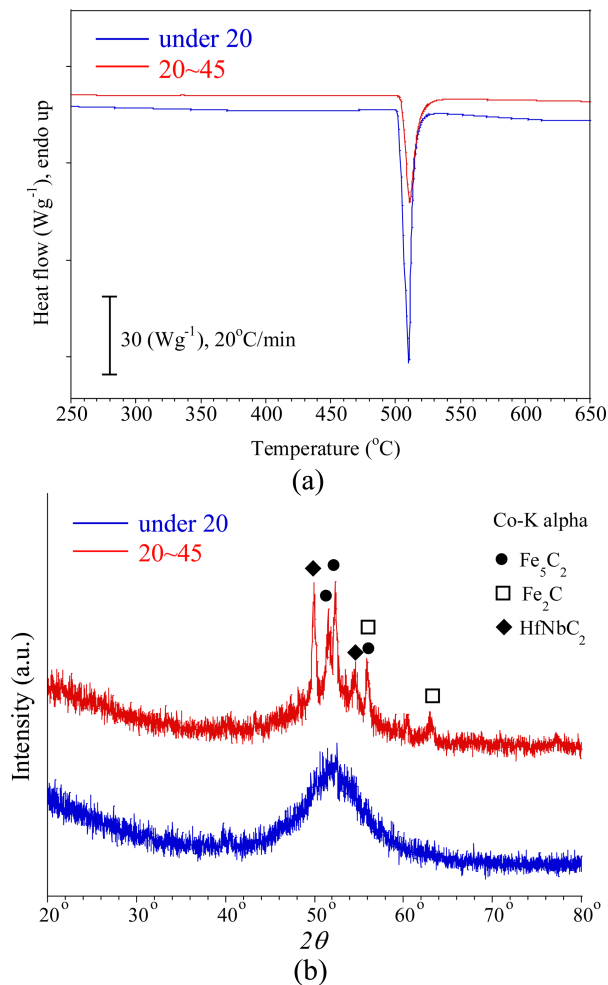
Fig. 2. (a) DSC trace (heating rate 20 K/min) of small-sized $Fe_{75}B_{13}P_5Nb_2Hf_1C_4$ alloy powders compared to large-sized alloy powders. (b) X-ray diffraction patterns of small-and large-sized $Fe_{75}B_{13}P_5Nb_2Hf_1C_4$ alloy powders.

faster than that of the large-sized powder when the melt entered the supercooled liquid region [$T_m \approx 1309$ K (1036 °C)]. The relative cooling rate difference was 12.7 between the small-sized powder (6.5×10^5 K/s) and the large-sized powder (5.1×10^4 K/s). However, the droplet temperature of the amorphous alloy down to T_x passed through the supercooled liquid region ($T_x \approx 781$ K), the cooling rate difference between the small-sized powder (1.3×10^4 K/s) and the large-sized powder (5.0×10^3 K/s) was 2.6. The cooling rate change difference during solidification from $T_{ejection}$ to T_x of the small-sized powder was 64.7, which was five times steeper than that of the large-sized powder (12.4).

Typical differential scanning calorimetry (DSC) traces

obtained during continuous heating at a rate of 20 K/min for the small- and large-sized gas-atomized powders (≤20 μm and 20-45 μm, respectively) are presented in Fig. 2(a). Both powders show a single exothermic reaction during heating, indicating that the amorphous phase crystallized through a single-stage process. In the DSC trace [Fig. 2(a)], the small-sized powder shows a glass transition temperature (T_g) of 472°C, a T_x onset temperature at 500°C, and a maximum exothermic crystallization peak temperature (T_p) at 510.4°C. A supercooled liquid range (ΔT_x) of 28°C and an integral heat of crystallization (ΔH_x) of 87.3 J/g were obtained at a heating rate of 20 K/min. The large-sized powder showed T_x at 498.2°C, T_p at 510.2°C, T_x of 26.2°C, and ΔH_x of 48.8 J/g. The large difference in crystallization enthalpy was discrete owing to the presence of a primary crystal phase in the amorphous matrix, which showed almost identical crystallization behavior with a single exothermic reaction during heating.

Fig. 2(b) shows the X-ray diffraction (XRD) patterns obtained from the gas-atomized $Fe_{75}B_{13}P_5Nb_2Hf_1C_4$ (at.%) amorphous powders. The XRD pattern obtained from the small-sized atomized powders exhibits a broad halo peak in the 2θ range of 40-60° in the Co-Ka wavelength (λ=0.1791 nm) and does not show any evidence of crystallization during gas atomization. For comparison, the XRD data from the large-sized as-atomized powder, shown in Fig. 2(b), exhibits visible Bragg reflections. The peaks are indexed to Fe_5C_2, Fe_2C, and $HfNbC_2$. These peaks coexist with diffuse scattering of comparable intensity, indicating that the amount of crystalline phases is low compared to that of the amorphous matrix. These crystalline peaks have been shown to occur during gas atomization as a result of the slow cooling rate. An estimate of the fraction of the crystalline phase in the gas-atomized $Fe_{75}B_{13}P_5Nb_2Hf_1C_4$ powders was made by comparing the crystallization enthalpy with other smaller-sized (≤20 μm) powders that did not show any Bragg reflections. From this comparison, the estimated fraction of the crystalline phase was approximately 29%. Crystalline peaks corresponding predominantly to $HfNbC_2$, along with minor reflections from the Fe_5C_2 and Fe_2C phases, were present in the amorphous matrix.

Fig. 3(a) shows a transmission electron microscopy (TEM) micrograph prepared by focused ion beam (FIB) method of the as-atomized small-sized powder obtained
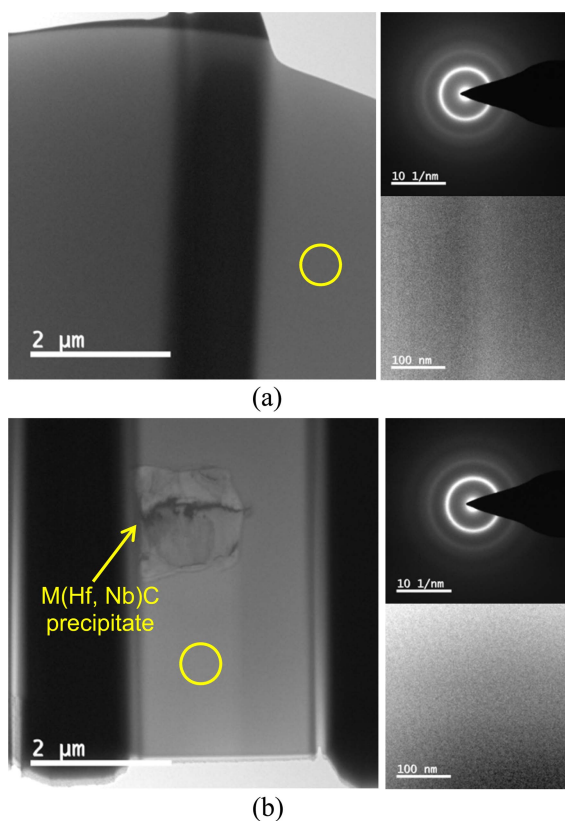
Fig. 3. Bright-field (BF) TEM image of the cross-sectional view of (a) small-sized and (b) large-sized amorphous powder prepared by focused ion beam (FIB) and inset SAD pattern with high-magnification TEM image obtained from yellow marked region.
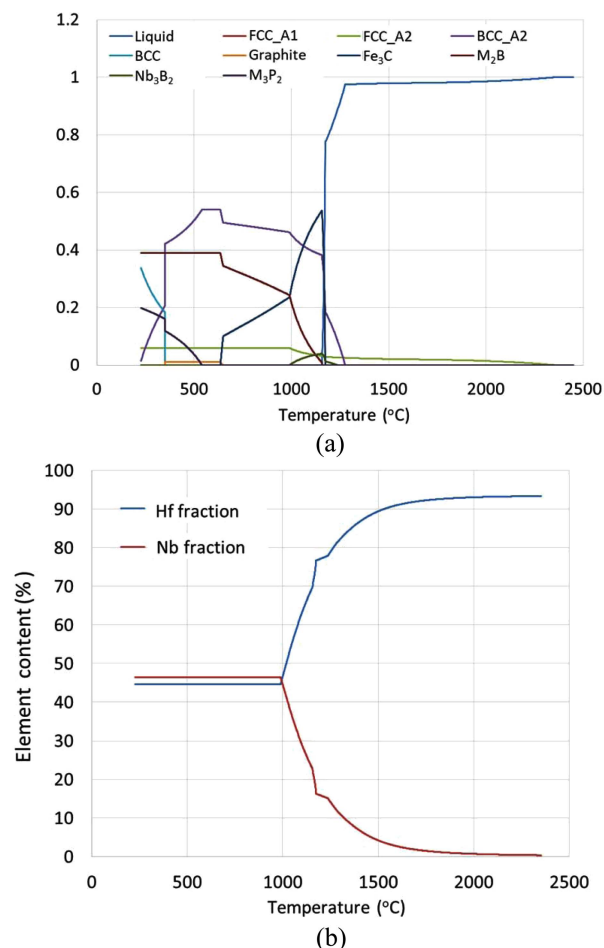

Fig. 4. (a) Crystallization of precipitates and equilibrium-phases fraction calculated by using MatCalc for $Fe_{75}B_{13}P_5Nb_2Hf_1C_4$ alloy. (b) Change of equilibrium solubility between Hf and Nb in M(Hf, Nb)C precipitate as a function of temperature change.

from the fast-cooled powder. The inset shows the selected-area diffraction (SAD) pattern and a higher-magnification TEM image obtained from the yellow circled region. The typical fully amorphous structure exhibits a broad halo contrast without any crystalline fringes. Fig. 3(b) shows a TEM image of the as-atomized large-sized powder obtained from the slow-cooled powder. The inset SAD pattern and higher-magnification TEM image shows a rectangular-shaped primary crystal surrounded by an amorphous matrix. These carbides with particle sizes of approximately ~1 μm are thought to be primary MC carbides. Table 1 shows the TEM energy dispersive spectrometer (EDS) mapping results of the atomized powder with slow cooling. The concentrations of Hf and Nb in the carbide are much higher than those in the matrix.

Fig. 4 shows the equilibrium phase fraction of the $Fe_{75}B_{13}P_5Nb_2Hf_1C_4$ alloy during solidification at a 10^4 K/s cooling rate, as calculated using the thermodynamic-based

software MatCalc [12]. Precipitation of the primary carbide occurs during cooling at 2354°C, where the liquid phase and solid primary phase coexist and the residual liquid phase completely transforms into a solid phase with multiple phases at 1157°C during further cooling. From the MatCalc calculation, the composition of MC carbide at 1071°C was determined to be 0.13Fe-58.8Hf-33.0Nb-8.07C wt.% (0.17Fe-24.24Hf-26.14Nb-49.45C at.%). The Hf fraction in the MC carbide decreases, whereas the Nb fraction in the MC carbide increases during cooling. The equilibrium contents of Hf and Nb at 1071°C in the phase diagram are 58.8 wt.% (24.2 at.%) and 33.0 wt.% (26.1 at.%), respectively. The composition of MC carbide formed at 1071°C has a chemical stoichiometry similar to that of

Table 1. EDS chemical composition analysis results for large-sized $Fe_{75}B_{13}P_5Nb_2Hf_1C_4$ gas-atomized powders.

at.%	Fe	P	Nb	Hf	C
Matrix	83.5±0.91	7.06±0.58	1.02±0.36	0.03	8.39±1.25
Precipitate1	5.71±0.27		28.48±1.57	22.43±0.93	43.38±3.89
Precipitate2	8.845		27.5	27.92	35.66

the precipitate obtained by TEM EDS analysis, as shown in Table 1.

4. Conclusion

In conclusion, we evaluated the critical cooling rate effect on the formation of the primary precipitate during gas atomization by freezing an alloyed melt at supercooled liquid temperature to prevent further crystallization or growth. The important observation from XRD diffraction and TEM results is that the structures of the as-atomized powders were similar to that of the amorphous matrix except for carbide formation during solidification of the large-sized powder owing to the slow cooling rate, indicating that the large-sized powder retained an amorphous state without further significant devitrification of the $Fe_{75}B_{13}P_5Nb_2Hf_1C_4$ matrix during adjustable cooling.

Acknowledgments

References

[1] D. A. Porter and K. E. Easterling, Phase transformations in metals and alloys, Chapman & Hall, New York (1992) 185.

[2] Kim SY, Oh HR, Kim HA, Lee AY, Kim HJ, Yang SS, Kim YJ, Choi HJ, Kim IH, J. Eckert, Kim JR and Lee MH, J. Appl. Phys., **126**(16) (2019) 165109.

[3] D. Turnbull, Contemp. Phys., **10**(5) (1969) 473.

[4] M. D. Ediger, C. A. Angell and S. R. Nagel, J. Phys. Chem., **100**(31) (1996) 13200.

[5] P. G. Debenedetti and F. H. Stillinger, Nature, **410** (2001) 259.

[6] G. Zhang, F. H. Stillinger and S. Torquato, Sci. Reports, **6** (2016) 36963.

[7] B. Zheng, Y. Lin, Y. Zhou and E. J. Lavernia, Metall. Mater. Trans. B, **40** (2009) 768.

[8] H. Shiwen, Y. Liu and S. Guo, Rare Met. Mater. Eng., **38** (2009) 353.

[9] Lee ES and Ahn S, Acta Metall. Mater., **42**(9) (1994) 3231.

[10] M. Yan, J. Q. Wang, G. B. Schaffer and M. Qian, J. Mater. Res., **26**(7) (2011) 944.

[11] A. Inoue and J. S. Gook, Mater. Trans. JIM, **36**(9) (1995) 1180.

[12] Park H, Park D, Jun JH, Lee MH and Lee SJ, Mater. Res. Express, **4** (2017) 116504.